J. Fluid Mech. (1999), *vol.* 380, *pp.* 257–278. Printed in the United Kingdom

© 1999 Cambridge University Press

Properties of large-amplitude internal waves

By JOHN GRUE, ATLE JENSEN, PER-OLAV RUSÅS AND J. KRISTIAN SVEEN

Mechanics Division, Department of Mathematics, University of Oslo, Norway

(Received 28 April 1998 and in revised form 17 August 1998)

Properties of solitary waves propagating in a two-layer fluid are investigated comparing experiments and theory. In the experiments the velocity field induced by the waves, the propagation speed and the wave shape are quite accurately measured using particle tracking velocimetry (PTV) and image analysis. The experiments are calibrated with a layer of fresh water above a layer of brine. The depth of the brine is 4.13 times the depth of the fresh water. Theoretical results are given for this depth ratio, and, in addition, in a few examples for larger ratios, up to 100:1. The wave amplitudes in the experiments range from a small value up to almost maximal amplitude. The thickness of the pycnocline is in the range of approximately 0.13–0.26 times the depth of the thinner layer. Solitary waves are generated by releasing a volume of fresh water trapped behind a gate. By careful adjustment of the length and depth of the initial volume we always generate a single solitary wave, even for very large volumes. The experiments are very repeatable and the recording technique is very accurate. The error in the measured velocities non-dimensionalized by the linear long wave speed is less than about 7–8% in all cases. The experiments are compared with a fully nonlinear interface model and weakly nonlinear Korteweg–de Vries (KdV) theory. The fully nonlinear model compares excellently with the experiments for all quantities measured. This is true for the whole amplitude range, even for a pycnocline which is not very sharp. The KdV theory is relevant for small wave amplitude but exhibit a systematic deviation from the experiments and the fully nonlinear theory for wave amplitudes exceeding about 0.4 times the depth of the thinner layer. In the experiments with the largest waves, rolls develop behind the maximal displacement of the wave due to the Kelvin–Helmholtz instability. The recordings enable evaluation of the local Richardson number due to the flow in the pycnocline. We find that stability or instability of the flow occurs in approximate agreement with the theorem of Miles and Howard.

1. Introduction

Signatures of internal waves propagating in a layered ocean or fjord have been observed at several locations, see e.g. the descriptions by Fjeldstad (1964), Farmer & Smith (1980), Gjevik & Høst (1984) and Apel *et al.* (1985). Internal waves are reported to have quite large amplitudes, up to the order of 100 m, and may locally introduce strong slowly varying currents in the ocean or in the fjord. Such induced currents may determine the dimensioning parameters of the risers of floating offshore platforms which are operating in deep water in areas where internal waves may occur. Knowledge of properties of internal waves and the loads they may cause is also relevant to the Submerged Floating Tunnel project in Rogaland in Norway.

There is a general need for mathematical models of large-amplitude internal waves

https://doi.org/10.1017/S0022112098003528 Published online by Cambridge University Press

propagating along an arbitrary pycnocline and the effects induced on marine structures. With regard to the wave modelling, the development of fully nonlinear two-layer models, where two homogeneous fluid layers are separated by an interface, have been the most extensive. Relevant references are Holyer (1979), Meiron & Saffman (1983), Turner & Vanden-Broeck (1986) in the case of periodic waves, and Amick & Turner (1986), Turner & Vanden-Broeck (1988), Evans & Ford (1996) in the case of solitary waves. Recently, Grue *et al.* (1997) used a time-stepping method for computing unsteady fully nonlinear interfacial waves to investigate upstream influence in trans-critical two-layer flow and the generation of solitary waves. It was found that a moving body generated upstream disturbances with amplitudes of the order of the depth of the thinner of the two layers, a result which was true even for bodies with small height imposing only weak forcing. The waves were clearly outside the ranges of validity of weakly nonlinear theories like the Korteweg–de Vries (KdV) theory (Keulegan 1953; Long 1956), the finite-depth theory (Kubota, Ko & Dobbs 1978) and the Benjamin–Ono theory (Benjamin 1967; Ono 1975). When the height of the body became too small, the upstream influence disappeared.

This remarkable finding, and more generally, the large differences between weakly nonlinear and fully nonlinear interface methods for moderate- and large-amplitude waves, as noted by several authors, have motivated us to set up experiments with the purpose of a general comparison with theory and to broaden our understanding of the propagation properties of internal waves. Relevant to our experiments are the works by Koop & Butler (1981), Segur & Hammack (1982) and Kao, Pan & Renouard (1985). In Koop & Butler, using water above freon, and in Segur & Hammack, using fresh water above salt water, they characterized solitary waves in terms of their shape and the amplitude–wavelength relationship. They compared the experiments with KdV theory, finite-depth theory and Benjamin–Ono theory. Basically, both works concluded that the experimental results fitted well with KdV theory or higher-order extensions of it. They did not find good agreement between the experiments and the finite-depth theory or the Benjamin–Ono theory, except for very small wave amplitude. Kao *et al.* studied internal waves on a thin pycnocline and found that KdV theory compared well with their experiments, for several depth ratios between the layers, and for small, moderate and even rather large amplitudes.

In our experiments we consider solitary waves propagating in a two-layer fluid consisting of fresh water above salt water. The depth of the lower layer is 4.13 times that of the upper layer in all experiments. We briefly give a few theoretical results for other depth ratios, with the purpose of broadening the picture. We perform experiments for wave amplitudes ranging from a small value up to the maximal. The investigation is facilitated by the recent progress of the optical particle tracking velocimetry method (PTV) which is a low-intensity mode of particle image velocimetry (PIV), see e.g. Adrian (1991). We shall here use the PTV method developed by Dalziel (1992) to measure the properties of the waves. We have also applied the PIV method in a few examples, giving the same results as with PTV. We quite precisely measure the entire velocity field induced by the waves, the propagation speed and the wave shape. All measurements are compared with the fully nonlinear two-layer model and with the KdV theory, the latter where appropriate. We shall find a surprisingly good agreement between the measurements and the fully nonlinear two-layer model for the whole range of wave amplitudes. The agreement is good even for a pycnocline which is not very sharp. The amplitude range where the KdV theory is valid is found to be rather small, and the theory becomes irrelevant for moderate and large amplitude.

An interesting aspect of comparing the theoretical and the experimental approaches

https://doi.org/10.1017/S0022112098003528 Published online by Cambridge University Press

is that the former may be used to check the PTV method. Since the fully nonlinear theoretical model can produce results with high precision, it provides a reference for the PTV method in the cases when the experimental conditions fit with the assumptions of the theory.

The paper is organized as follows: following this Introduction, §2 describes the experimental set-up, the generation of waves, the optical method and an analysis of its accuracy in the present experiments. We calibrate initial conditions which lead to a single solitary wave, even for very large initial volumes. In §3 the fully nonlinear two-fluid model, the KdV model and waves with a theoretical maximal amplitude are described. Results for the velocity profile at the maximal displacement of the wave are presented in §4. In §5 we give results for the propagation velocity, and in §6 for the wave profile. Finally, §7 is a conclusion.

2. Experimental set-up and method

2.1. *Filling of the tank and generation of waves*

The experiments were carried out in the Hydrodynamical Laboratory at the University of Oslo. A wave tank 0.5 m wide and either 6.2 or 12.3 m long was used. In one run we also used a tank length of 21.4 m. The calibration of each experiment starts by preparing a lower layer of brine with density $\rho_1 = 1.022\ldots$ g cm^{-3} and depth h_1. When the brine has become homogeneous, a layer of fresh water of depth h_2 and density $\rho_2 = 0.999\ldots$ g cm^{-3} is very gently filled on top of the lower layer, through fleets with sponges, during a time period of up to 6 hours. The density profiles are recording with a Yokogawa SC12 meter, which determines the density from the local conductivity of the fluid. Reference measurements are then taken at some selected locations using a Mettler-Toledo DA-300M density meter which determines the density with four decimal places. The values of ρ_1 and ρ_2 are allowed to vary in the fourth decimal from run to run due to practical reasons. Such a variation has a small influence on the measured velocities, but when we divide the results by the linear long wave speed c_0, the density variations from run to run become unimportant. The speed c_0 is determined theoretically by (3.8).

To generate waves we gently add a volume of fresh water behind a gate which is lowered at one end of the tank. A corresponding mass of the brine then slowly moves to the other side of the gate such that hydrostatic balance is maintained. The depths of the layers in the main part of the tank are in each experiment $h_1 = 62$ cm and $h_2 = 15$ cm, while the initial volume of fresh water behind the gate is varied. We have also performed one run with $h_1 = 31$ cm and $h_2 = 7.5$ cm. By removing the gate, an initial depression develops into a leading solitary wave propagating ahead of a transient dispersive wave train. Here we shall focus on initial conditions leading to a single solitary wave. We use the same generation procedure as that of Kao *et al.* (1985), who performed investigations generating either a single solitary wave or a train of solitary waves. At the other end of the tank the waves are reflected by a vertical wall. The waves generated move back and forth for quite a long time before they are damped out. A sketch of the experiment is presented in figure 1.

If we remove a certain volume of the upper layer behind the gate, instead of adding fresh water, a train of internal dispersive waves is generated, with no leading solitary wave. We do not, however, give results for this case here.

2.2. *The optical method*

The wave properties are determined using PTV. This method is well suited to our experiments due to the relatively small accelerations induced by the waves, and we

https://doi.org/10.1017/S0022112098003528 Published online by Cambridge University Press

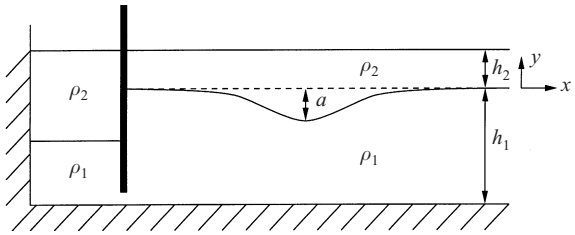


FIGURE 1. Sketch of the wave tank.

shall generally find a very good accuracy of the measurements. The first step is to illuminate the vertical section(s) of the fluid prepared for recording. In each section we create one light sheet with thickness 5 cm at a distance of 10 cm from the glass wall of the tank. The light sheet is vertical and parallel to the side of the tank. In the long tank two sections are illuminated, at mean positions 4.5 m and 10.4 m, respectively, from the wall at the upper end of the tank, in the end where the wave begins. In the short tank only the section at 4.5 m is used. Powerful overhead projectors are used as light sources.

In the next step the illuminated sections are seeded with small particles. We use particles of pliolite VTAC, a granular material used in white paint, with good reflective properties and density approximately 1.0228 g cm^{-3}. The appropriate size of the particles is obtained by crushing and seiving the pliolite. The particles are then put into a wetting agent for some time to reduce the effect of surface tension. By carefully adjusting the time of the treatment we obtain particles which effectively are neutrally buoyant for all values of the density profile.

The experiments are recorded by two monochrome COHU 4912 CCD cameras with a resolution of 575 $\times$ 560 pixels. The size of the particles is adjusted according to the resolution of the cameras such that a particle at rest normally is covered by four pixels.

In most of the cases we record the fluid motion in sections of the light sheets approximately 50 cm long and 40 cm high, using particles of diameter 800–1000 μm. We have also recorded the fluid motion in sections of 40 cm $\times$ 30 cm using particles of size 600–900 μm, to improve the accuracy of the measurements in the upper fluid (figure 2 *c*). We also sometimes record the motion in a larger section of 80 cm $\times$ 60 cm (figure 2 *a*,*c*) using particles of size 1000–1500 μm. We get the same results using the three different close-ups of the flow. Highest accuracy is always obtained for the finest resolution, as expected.

Each cell in the CCD-chip is charged for 1/50 s. The even and odd lines of the register are transmitted sequentially to the video tape in such a manner that in each frame the signals in the odd lines have a time lag of 1/100 s compared to the signals in the even lines. This gives an effective shutter speed of 3/100 s, while the time between each frame is 1/25 s. In the experiments we observe a maximal velocity of about 10 cm s^{-1}. (The speed is somewhat higher for the largest waves.) A particle with such a velocity moves about three times the length of a pixel during 3/100 s. This explains why the image analysis exhibits individual particles covering up to about eight pixels. In an attempt to increase the accuracy, we have made some recordings using a mechanical shutter in front of the cameras, giving an exposure time of 1/100 s. This decreases the light intensity of the particles too much, however, and we did not use this arrangement here.

After each run a Perspex plate with reference coordinates was submerged to the

https://doi.org/10.1017/S0022112098003528 Published online by Cambridge University Press

fluid and recorded. Special reference points are always mounted on the wave tank. The mapping between the recording section and the camera is linear.

The video frames are digitized using a frame-grabber card with a resolution of 512 by 512 pixels, covering the intermediate lines of the CCD-chip, and with grey scale from 1 to 256. We require that the picture of a particle shall cover at least three pixels and have intensity level in the interval from 25 to 80, to be accepted. Typically we identify 800–2500 particles in each frame. The information in sequences of pictures is then analysed. For this purpose we use the DigImage program developed by Dalziel (1992). First the area centroid of each particle in the single frames is determined. The particles in subsequent frames are then paired using an extension of the transport algorithm (Hichcock 1941). The displacement, velocity and trace of each particle are determined from sequences of five frames, which means that each particle is traced for 0.2 s. A longer tracing interval introduces loss of particles. Further details of the experimental set-up and method are given in Sveen, Jensen & Grue (1998).

2.3. *Relative accuracy of the optical method*

The first question to be answered is: how close is the velocity $\boldsymbol{V}$ of a particle to the surrounding fluid velocity $\boldsymbol{v}(\boldsymbol{x}, t)$? The particles are neutrally buoyant and have approximately spherical shape. As we use relatively small particles in the experiments we may assume that viscosity dominates the effect of inertia of the fluid. This means that the force acting on a particle may be approximated by the Stokes drag, i.e. $\boldsymbol{D} = 6\pi\rho\nu R(\boldsymbol{v} - \boldsymbol{V})$, where ν denotes kinematic viscosity and R radius of the particle. Balance of momentum of the particle then gives

$$|\boldsymbol{v} - \boldsymbol{V}| = \alpha|\dot{\boldsymbol{V}}|, \tag{2.1}$$

where

$$\alpha = \frac{(4\pi/3)\rho R^3}{6\pi\rho\nu R} = \frac{2R^2}{9\nu}. \tag{2.2}$$

In the present experiments we have that $|\dot{\boldsymbol{V}}| \sim |\boldsymbol{V}|_{max}/T$ where a typical value of T is in the interval 5–10 s. With $R = 0.5$ mm and $\nu = 10^{-6}$ m^2 s^{-1} we find

$$\frac{|\boldsymbol{v} - \boldsymbol{V}|}{|\boldsymbol{V}|_{max}} \sim \frac{2R^2}{9\nu T} \sim 0.005 - 0.01. \tag{2.3}$$

We note that the particle Reynolds number, $Re = 2R|\boldsymbol{v} - \boldsymbol{V}|/\nu$, becomes less than unity for $|\boldsymbol{V}|_{max}$ less than 10 cm s^{-1}. Thus, the seeded particles quite closely follow the fluid motion, with an accuracy determined by (2.3).

The next question is: what is the accuracy of the image processing technique in determining the particle velocities? From the discussion above we may assume that the position and displacement of each particle is determined with an accuracy better than the length of a pixel, which for the 50 cm $\times$ 40 cm section is about 1 mm. (Dalziel 1992 found in his experiments that that the position of a particle is determined with an accuracy of about 0.2 times the pixel length.) As already mentioned, the trace of a particle and its displacement are obtained from a sequence of five frames during a time interval of 0.2 s. A particle with velocity 10 cm s^{-1} then moves a distance of 2 cm, which means that the relative error in the particle displacement and the velocity is at most 1 mm/2 cm = 5%. This is a much larger figure than in (2.3).

Additional error sources exist, including e.g. inhomogeneities in the experimental set-up, inhomogeneous distribution of particles, local effect of surface tension at the free surface and incorrect pairing of particles. We shall see, however, that the relative

https://doi.org/10.1017/S0022112098003528 Published online by Cambridge University Press

error in the measured velocities is approximately in agreement with the error analysis just described.

The measurements presented are based on recorded data somewhat away from the vertical boundaries of the images, where particles may appear or disappear, and lens aberration is at its largest, to avoid further uncertainties.

3. Theoretical two-layer models

We calibrate the experiments with a relatively sharp pycnocline and shall compare the measurements with theoretical two-layer models. The thin pycnocline is then replaced by an interface separating the upper and lower fluid. The theoretical models include the fully nonlinear theory and weakly nonlinear Korteweg–de Vries (KdV) theory. A comparison between experiments and theory provides a useful evaluation of the latter and illustrates its domain of validity. On the other hand, such a comparison also provides an evaluation of the accuracy of the optical method when the experimental conditions fit with the assumptions of the theory.

3.1. *Fully nonlinear model for two-layer fluid*

As mentioned in the Introduction, fully nonlinear computations of wave profiles have previously been performed by Turner & Vanden-Broeck (1988). Furthermore, horizontal fluid velocities as a function of the depth in the 'crest plane' of the wave have been presented by Evans & Ford (1996). We have found it advantageous to apply a somewhat different nonlinear model than these authours. Our model is a type of fully nonlinear time-stepping method for interfacial waves (Grue *et al.* 1997) where the complex fluid velocities (see below) are obtained using Cauchy's theorem. We have used our model to recompute some of the waves and velocities presented by previous authors, finding the same results.

Solitary waves of permanent form are modelled in the frame of reference moving with the wave speed c. In this frame of reference the interface is 'frozen' and there is a horizontal current in the far field with velocity $-c$. We assume that in each layer the fluid is incompressible, homogeneous and inviscid, and the motion irrotational.

A coordinate system O, xy is introduced with the x-axis at the level of the interface in the far field and the y-axis pointing upwards. As we apply complex analysis, the complex variable $z = x+\mathrm{i}y$ and complex velocities $q_k(z) = u_k(x,y) - c - \mathrm{i}v_k(x,y)$ are introduced, where $k = 1, 2$ refer to the lower and upper layer, respectively. The components $u_k - c$ and v_k determine the horizontal and vertical velocities, respectively. Furthermore, q_1 and q_2 are analytic functions of z, according to the continuity equation. The kinematic boundary condition at the bottom of the lower fluid gives that $v_1 = 0$ at $y = -h_1$. Due to the slow speed of the interfacial waves there is almost no vertical motion of the free surface, and we may apply the rigid lid condition there, i.e. $v_2 = 0$ at $y = h_2$. We further note that $q_1, q_2 \to -c$ in the far field, and that there are no velocities normal to the interface (in this frame of reference).

The complex velocities are determined by applying Cauchy's integral theorem to $q_1 + c$ and $q_2 + c$. By following the procedure in Grue *et al.* (1997) we obtain

$$\mathrm{PV}\int_I \frac{q_1(z)+c}{z'-z}\mathrm{d}z + \int_I \frac{q_1^*(z)+c}{z^*-2\mathrm{i}h_1-z'}\mathrm{d}z^* = \begin{cases} 2\pi\mathrm{i}(q_1(z')+c), & z' \in \Omega_1 \\ \pi\mathrm{i}(q_1(z')+c), & z' \in I, \end{cases} \tag{3.1}$$

$$\mathrm{PV}\int_I \frac{q_2(z)+c}{z'-z}\mathrm{d}z + \int_I \frac{q_2^*(z)+c}{z^*+2\mathrm{i}h_2-z'}\mathrm{d}z^* = \begin{cases} -2\pi\mathrm{i}(q_2(z')+c), & z' \in \Omega_2 \\ -\pi\mathrm{i}(q_2(z')+c), & z' \in I, \end{cases} \tag{3.2}$$

https://doi.org/10.1017/S0022112098003528 Published online by Cambridge University Press

where we have applied the method of images. Furthermore, $q_k^*(z) = u_k(x,y) - c + \mathrm{i}v_k(x,y)$, an asterix denotes complex conjungate, PV denotes principal value, I the interface and Ω_k the domain of fluid k. We parameterize I by $z(\xi)$. The tangential velocities at I are determined by $\gamma_1/|z_\xi| = q_1 z_\xi/|z_\xi|$ and $\gamma_2/|z_\xi| = q_2 z_\xi/|z_\xi|$ where $z_\xi = \mathrm{d}z/\mathrm{d}\xi$. From (3.1)–(3.2) the following non-singular integral equations of Fredholm type of the second kind may be deduced:

$$\pi(\gamma_1' + cx_\xi') = \mathrm{PV}\int_I \mathrm{Re}\left(\frac{z_\xi'}{z'-z}\right) cy_\xi \mathrm{d}\xi - \int_I \mathrm{Re}\left(\frac{z_\xi'}{z^*-2\mathrm{i}h_1-z'}\right) cy_\xi \mathrm{d}\xi + \int_I \mathrm{Im}\left(\frac{z_\xi'}{z'-z} + \frac{z_\xi'}{z^*-2\mathrm{i}h_1-z'}\right)(\gamma_1 + cx_\xi)\mathrm{d}\xi, \quad z' \in I, \tag{3.3}$$

$$-\pi(\gamma_2' + cx_\xi') = \mathrm{PV}\int_I \mathrm{Re}\left(\frac{z_\xi'}{z'-z}\right) cy_\xi \mathrm{d}\xi - \int_I \mathrm{Re}\left(\frac{z_\xi'}{z^*+2\mathrm{i}h_2-z'}\right) cy_\xi \mathrm{d}\xi + \int_I \mathrm{Im}\left(\frac{z_\xi'}{z'-z} + \frac{z_\xi'}{z^*+2\mathrm{i}h_2-z'}\right)(\gamma_2 + cx_\xi)\mathrm{d}\xi, \quad z' \in I. \tag{3.4}$$

The pressure in each of the fluids is determined from the Bernoulli equation. Continuity of the pressure at the interface then gives

$$\frac{1}{2|z_\xi|^2}(\gamma_1^2 - \mu\gamma_2^2) - \tfrac{1}{2}(1-\mu)c^2 + (1-\mu)gy = 0 \quad \text{at } I, \tag{3.5}$$

where $\mu = \rho_2/\rho_1$ and g denotes the acceleration due to gravity. More details of the derivations may be found in Grue *et al.* (1997). The equations (3.3)–(3.5) are solved by an iterative scheme where in each step $\gamma_1(x)$, $\gamma_2(x)$, $y(x)$ and c are determined, given the amplitude or volume of the wave. We have performed all computations using (3.5) with $\mu = 0.9775$. The numerical implementation is described in the Appendix.

3.2. *Korteweg–de Vries model*

Various KdV models have been applied to investigate weakly nonlinear interfacial waves (Keulegan 1953; Long 1956; Koop & Butler 1981; Segur & Hammack 1982; Kao *et al.* 1985; Melville & Helfrick 1987) and it is relevant to compare with KdV theory also in our investigation. With the fully nonlinear model available (§3.1) we here only consider a low-order version of the KdV theory. The solitary wave solution for a depression with amplitude a, which is the case when $h_2 < h_1$, may be found in Long (1956, Part II):

$$\hat{\eta}(x,t) = -a\,\mathrm{sech}^2[(x-ct)/\lambda], \tag{3.6}$$

$$\frac{c}{c_0} - 1 = \frac{a(\rho_2 h_1^2 - \rho_1 h_2^2)}{2h_2 h_1(\rho_2 h_1 + \rho_1 h_2)}, \tag{3.7}$$

$$c_0^2 = \frac{g h_1 h_2(\rho_1 - \rho_2)}{\rho_2 h_1 + \rho_1 h_2}, \tag{3.8}$$

$$\frac{1}{\lambda^2} = \frac{3a[1 - \rho_1 h_2^2/(\rho_2 h_1^2)]}{4h_2^2 h_1(\rho_1/\rho_2 + h_2/h_1)}. \tag{3.9}$$

We shall be interested in the fluid velocity induced by the waves, and in particular in the velocity profile at the maximal depression. KdV theory gives for the velocity

https://doi.org/10.1017/S0022112098003528 Published online by Cambridge University Press

profile in the upper layer, i.e. for $0 < y < h_2$,

$$\frac{u_2(x=ct,y)}{c_0}=\left[-\frac{\hat{\eta}}{h_2}\left[1+\frac{\alpha(\rho_2h_1^2-\rho_1h_2^2)}{2h_1(\rho_2h_1+\rho_1h_2)}\right]-\frac{\hat{\eta}^2}{h_2^2}-\frac{h_2\hat{\eta}''}{6}+\frac{\hat{\eta}''(y-h_2)^2}{2h_2}\right]_{x=ct}+O(\alpha^3), \tag{3.10}$$

and in the lower layer, i.e. $-h_1 < y < 0$,

$$\frac{u_1(x-ct,y)}{c_0}=\left[\frac{\hat{\eta}}{h_1}\left[1+\frac{\alpha(\rho_2h_1^2-\rho_1h_2^2)}{2h_1(\rho_2h_1+\rho_1h_2)}\right]-\frac{\hat{\eta}^2}{h_1^2}+\frac{h_1\hat{\eta}''}{6}-\frac{\hat{\eta}''(y+h_1)^2}{2h_1}\right]_{x=ct}+O(\alpha^3), \tag{3.11}$$

where $(\,)' = \partial/\partial x$ and $\alpha = a/h_2$. The assumptions leading to (3.6)–(3.11), besides those described in §3.1, are $a/h_2 \ll 1$ and $(h_1+h_2)/\lambda \ll 1$.

We note that Koop & Butler (1981) has extended the KdV equation for internal waves to second order. The second-order correction gives, however, no effect on the velocity at the wave crest.

3.3. *Interfacial waves with maximal amplitude*

The speed and amplitude of interfacial solitary waves have theoretical upper bounds, c_{max} and a_{max}, respectively, when h_1 and h_2 are finite (Amick & Turner 1986). The volume of the wave may become infinitely large in this limit (Turner & Vanden-Broeck 1988). The formulae for c_{max} and a_{max} derived by Amick & Turner read

$$c_{max}^2=\frac{g(h_1+h_2)(\rho_1-\rho_2)}{(\rho_1^{1/2}+\rho_2^{1/2})^2}, \tag{3.12}$$

$$a_{max}=\frac{h_1\rho_2^{1/2}-h_2\rho_1^{1/2}}{\rho_1^{1/2}+\rho_2^{1/2}}. \tag{3.13}$$

We note that (3.12) may also be written

$$c_{max}^2=\frac{gh_1'h_2'(\rho_1-\rho_2)}{\rho_1h_2'+\rho_2h_1'}, \tag{3.14}$$

where $h_2' = h_2 + a_{max}$ and $h_1' = h_1 - a_{max}$ (with $h_2 < h_1$). The latter expression has precisely the same form as (3.8) for the linear long wave speed c_0^2, except that the local depths of the fluid layers are h_1' and h_2'.

The maximal fluid velocities which may be induced in each of the layers may then be determined by conservation of mass, giving

$$h_2c_{max}=h_2'(c_{max}-u_{2max}), \qquad h_1c_{max}=h_1'(c_{max}-u_{1max}). \tag{3.15}$$

The expressions for u_{2max} and u_{1max} become very simple if we use the Boussinesq approximation, which is a relevant approximation in view of the conditions in the experiments. In this approximation ρ_1/ρ_2 is put equal to unity except in the buoyancy term in the dynamic condition (3.5), and gives

$$\frac{u_{2max}}{c_0}=-\frac{u_{1max}}{c_0}=\frac{h_1-h_2}{2(h_1h_2)^{1/2}}. \tag{3.16}$$

4. Velocity profile at the maximal displacement of the wave

We now turn to the experiments where internal solitary waves with a depression, generated as described in §2.1, are propagating along the pycnocline. The particle

https://doi.org/10.1017/S0022112098003528 Published online by Cambridge University Press

imaging method is dedicated to velocity measurements, giving the fluid velocities of a section of the fluid as part of the output. We first examine the instantaneous velocity field at the maximal displacement of the pycnocline, with vertical coordinate $y_m = -a$ relative to the initial level of the pycnocline, and with horizontal coordinate moving with $x_m = ct$ (c is determined as described in §5). The horizontal velocity profile $u(y)$ at x_m is positive above the pycnocline, along the direction of the wave propagation, and negative below. With the rather abrupt change from a positive to a negative velocity, the vertical position of the pycnocline at the trough of the wave, and thereby the value of a, may be determined quite accurately from the measurements.

We have performed experiments with several initial conditions generating solitary waves with different amplitudes. Measured velocity profiles are presented in figure 2 for non-dimensional amplitude a/h_2 in the interval 0.22–1.35. Most of the measurements cover a vertical cut between the free surface and midway down the wave tank using the recording section of 50 cm × 40 cm (see §2.2). In two cases (figures 2*a* and 2*c*) a larger section of the flow is also recorded, giving velocity profiles for almost the entire vertical domain.

The results for the upper layer exhibit a pronounced horizontal velocity with only a weak dependence of the vertical coordinate. The velocity below the pycnocline is small when a is small but becomes as pronounced as in the upper layer when a/h_2 becomes of the order of unity or larger.

The experiments are very repeatable, as documented in figure 2(*c*), where results for $a/h_2 \simeq 0.78$ from ten different runs with approximately the same conditions are displayed. The initial volume of fresh water is in all cases the same. Five of the runs are performed with a pycnocline thinner than about 2 cm, with the preparation as described in §2.1. Each of the remaining runs are performed after a previous run without preparing a new upper layer. The pycnocline is then somewhat thicker due to the mixing occurring in the previous experiment. The results in figure 2(*c*) exhibit an overall unique picture of the velocity profile, even for slightly different shapes of the pycnocline. The density profiles are determined as descibed in §2.1 before each run, and some examples of the conductivity measurements are displayed in figure 2(*f*). We notice that the transition from a positive to a negative velocity is abrupt for a discontinuous density profile and smooth for a smooth density profile.

4.1. *Waves with almost maximal amplitude*

It is of interest to try to generate waves with displacement close to the maximal amplitude predicted by the two-layer model described in §3.3, and to investigate the corresponding velocity profiles. In this case a large initial volume has to be used. We have made several attempts in our wave tank using different initial volumes, different total depths of the fluid and different lengths of the tank. First the standard calibration (case A) is used, with $h_2 = 15$ cm, $h_1 = 62$ cm and length of the tank $L = 12.3$ m. The thickness of the pycnocline is approximately 2 cm and the initial volume is 2 m × 0.4 m × 0.5 m. Next we calibrate an experiment with $h_2 = 7.5$ cm, $h_1 = 31$ cm, $L = 12.3$ m, pycnocline thickness approximately 2 cm and initial volume 1 m × 0.2 m × 0.5 m (case B). Finally we use a larger part of the wave tank with $h_2 = 15$ cm, $h_1 = 62$ cm, $L = 21.4$ m, pycnocline thickness approximately 2 cm and initial volume 2 m × 0.4 m × 0.5 m (case C). The motion is recorded in sections with mean positions 6.5 m (different from the previous runs) and 10.4 m from the upper end of the tank. In case C recordings are also made at a position at 14.5 m.

We measure the largest negative displacement $|y|_{max}/h_2 \simeq 1.45$ in case A, $|y|_{max}/h_2 \simeq 1.45$ in case B and $|y|_{max}/h_2 \simeq 1.50$ in case C, where the latter is fairly close to the

https://doi.org/10.1017/S0022112098003528 Published online by Cambridge University Press

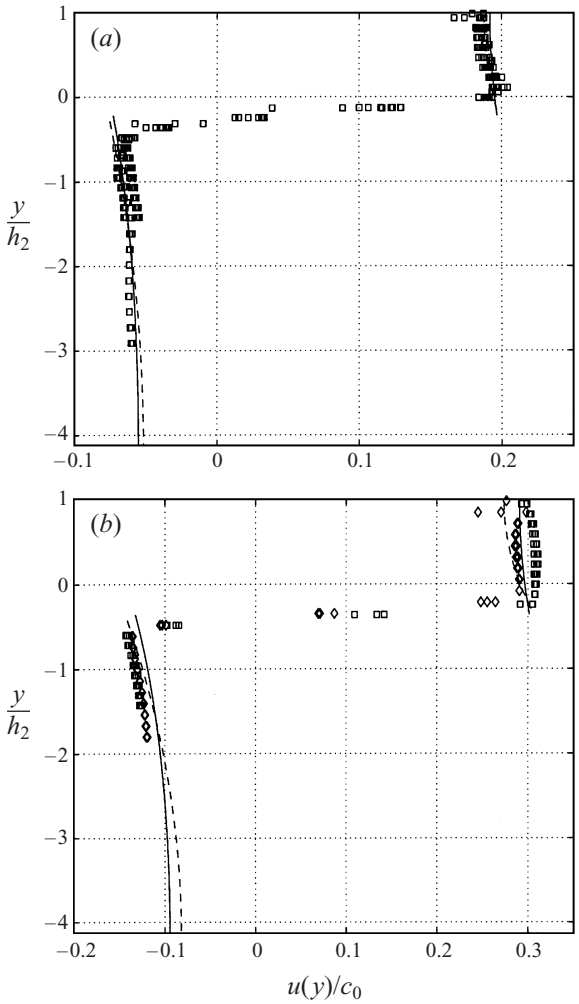


FIGURE 2(*a*, *b*). For caption see page 268.

maximal amplitude $a_{max}/h_2 \simeq 1.55$ predicted by (3.13). The propagating disturbances introduce velocity profiles which are displayed in figure 3(*a*,*b*). The results in figure 3(*a*) are very close to the maximal velocities predicted by (3.16). The velocity in the lower layer becomes somewhat reduced as the wave propagates along the tank according to the small decay of the amplitude.

While figure 3(*a*) exhibits a velocity profile with a jump, the change in the velocity profile at the pycnocline is more gradual in figure 3(*b*). In the latter case, the velocities in the lower layer fit well with the two-layer model. The velocities in the upper layer are, however, larger in the upper part and smaller in the lower part of the layer, than what is predicted by theory. This is more pronounced at camera 2 (at 10.4 m) than at camera 1 (at 6.5 m). This run is calibrated using the standard procedure, but with h_2=7.5 cm and h_1=31 cm, i.e. half of the usual fluid depths. We are, however, not able to reduce the nominal thickness of the pycnocline accordingly, which means that the relative thickness of the pycnocline in case B is about twice that in cases A and C. There is no stratification in the upper layer. The shape of the velocity

https://doi.org/10.1017/S0022112098003528 Published online by Cambridge University Press

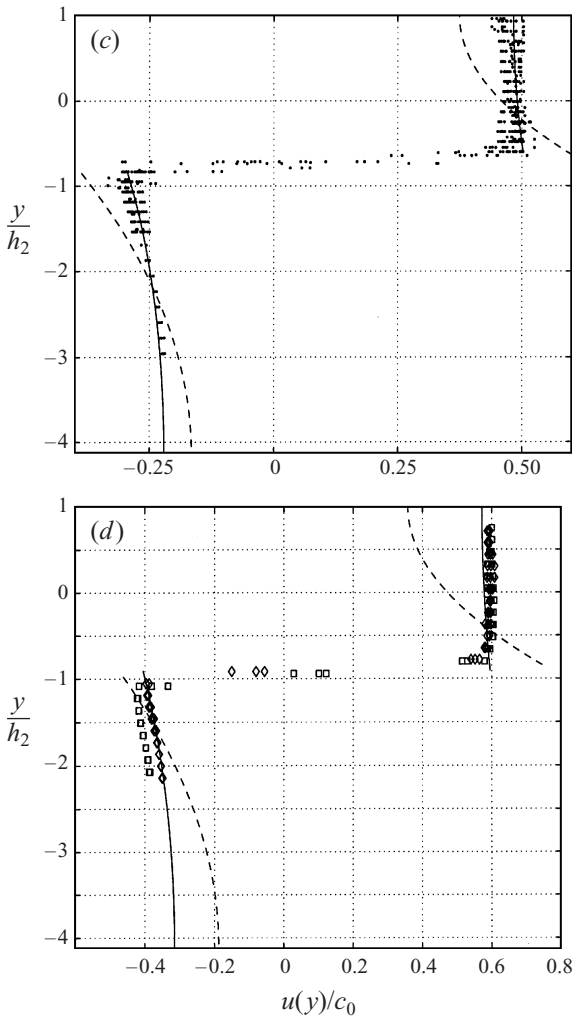


FIGURE 2(*c*, *d*). For caption see next page.

profile in figure 3(*b*) is thus attributed to the relatively thicker pycnocline in this case. Other experiments (not shown here) with a still thicker pycnocline exhibit the same tendency, but more pronounced.

The leading part of the wave profile is stable in all cases A–C. We observe, however, that rolls due to the Kelvin–Helmholtz instability develop on the pycnocline behind the maximal negative displacement in cases A and C. We have observed such instability in a few other runs (made for the purpose of visualization without making measurements). These runs are characterized by a large wave propagating along a very thin pycnocline. In case B, with a relatively thicker pycnocline and smaller velocity shear than in cases A and C, instability is not observed.

When instability takes place in the experiments it is evident that the destabilizing effect of an unstable velocity profile dominates the stabilizing effect of the stable density profile. The inverse ratio between these effects is expressed in terms of the Richardson number $Ri = g\beta/(\partial u/\partial y)^2$ where $\beta = -(\partial\rho/\partial y)/\rho$. According to Miles (1961) and Howard (1961) a sufficient condition for the stability of a stratified flow

https://doi.org/10.1017/S0022112098003528 Published online by Cambridge University Press

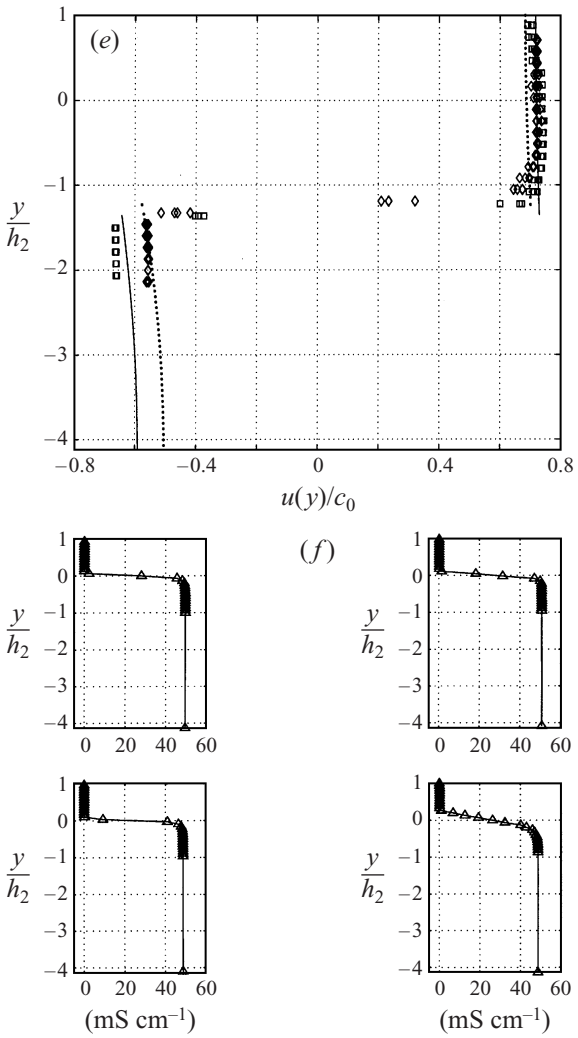


FIGURE 2. Velocity profile $u(y)/c_0$ at the maximal displacement of the wave vs non-dimensional vertical coordinate. c_0 determined from (3.8). Squares or dots: measurements at camera 1. Diamonds: measurements at camera 2. Solid line: Fully nonlinear theory. Dashed line in *a–d*: KdV theory, (3.10)–(3.11). (*a*) $a/h_2 = 0.22$. (*b*) $a/h_2 = 0.39$ (camera 1), $a/h_2 = 0.36$ (camera 2). (*c*) $a/h_2 = 0.78$. (*d*) $a/h_2 = 0.91$.(*e*) $a/h_2 = 1.35$ (camera 1) and 1.23 (camera 2, dotted line). (*f*) Initial conductivity profiles measured in mSiemens/cm for some of the examples in (*c*).

is that the Richardson number everywhere should exceed $\frac{1}{4}$. We may determine $\partial u/\partial y$ from the velocity measurements, $\partial \rho/\partial y$ from the initial density profile and then estimate the value of *Ri* within the pycnocline for the various runs. The results presented in table 1 are roughly in agreement with the theorem of Miles and Howard. The accuracy of the estimates would be enhanced if the actual density gradient during the wave motion could be measured.

4.2. *Comparison with theory*

Theoretical velocity profiles are obtained by the fully nonlinear theory described in §3.1, and by the KdV theory, (3.10)–(3.11). The fully nonlinear theory and the

https://doi.org/10.1017/S0022112098003528 Published online by Cambridge University Press

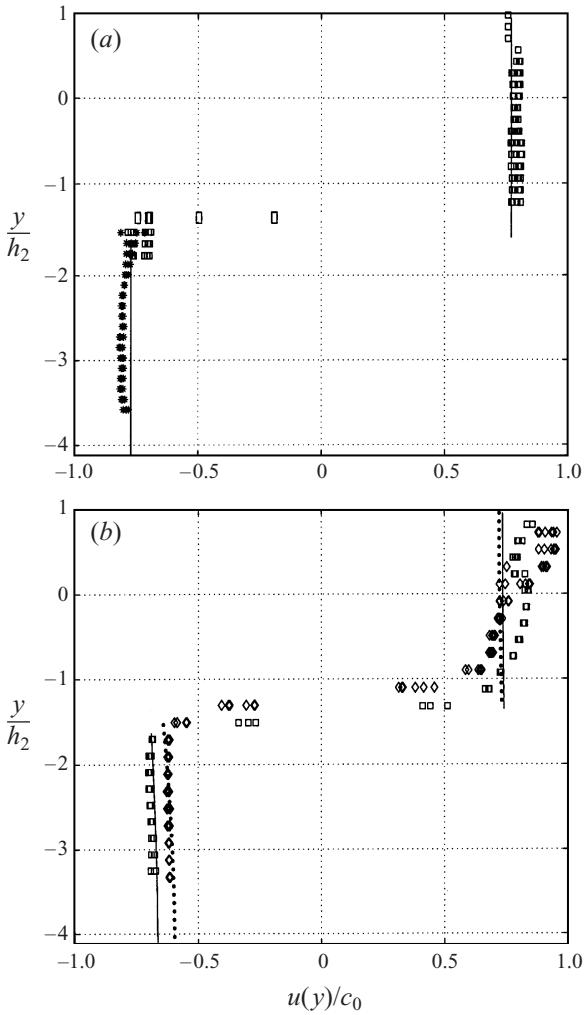


FIGURE 3. Velocity profile $u(y)/c_0$ at the maximal displacement of the wave vs non-dimensional vertical coordinate. Almost maximal amplitude. c_0 determined from (3.8). Squares and stars: measurements at camera 1 (6.5 m). Diamonds: measurements at camera 2 (10.4 m). (*a*) Case A (measurements in the upper layer) and case C (measurements in the lower layer). Solid line: (3.16). (*b*) Case B. Fully nonlinear theory, solid line: $a/h_2 = 1.45$ dotted line: $a/h_2 = 1.35$

measured velocity profiles exhibit very good agreement for all examples in figures 2–3. We find that the KdV theory is good for small a/h_2 (figure 2*a*,*b*) but becomes less useful for moderate and large wave amplitude (see figure 2*c*,*d* and figures below).

We further investigate the velocity $u_2(y = h_2/2)$ in the upper layer and the velocity $u_1(y = -a^-)$ in the lower layer just below the pycnocline, as functions of the non-dimensional amplitude. Results from all our experiments are shown in figure 4(*a*,*b*). (In the KdV theory we evaluate $u_1(y = 0^-)$, which is consistent within the approximations made in (3.11).) The measurements exhibit a quite marked trend, and again the very good agreement between the fully nonlinear theory and the measurements for the whole amplitude range is illustrated. The KdV model is appropriate only for small a/h_2, on the other hand.

We have so far only considered a depth ratio of 4.13 between the layers. It is

https://doi.org/10.1017/S0022112098003528 Published online by Cambridge University Press

Figure	2(*d*)	2(*e*)	3(*a*)	3(*b*)
$\partial(u/c_0)/\partial(y/h_2)$	3.3	6.3	11.0	4.0
Ri	0.85	0.23	0.07	0.58
Instability observed	No	No	Yes	No

TABLE 1. Estimated Richardson number from the experimental data presented in figures 2(*d*,*e*), 3(*a*,*b*). $\partial u/\partial y$ is estimated from the velocity measurements. Slope of ρ obtained by $\Delta\rho/\Delta y$, where $\Delta y \sim 2$ cm is the estimated initial thickness of the pycnocline.

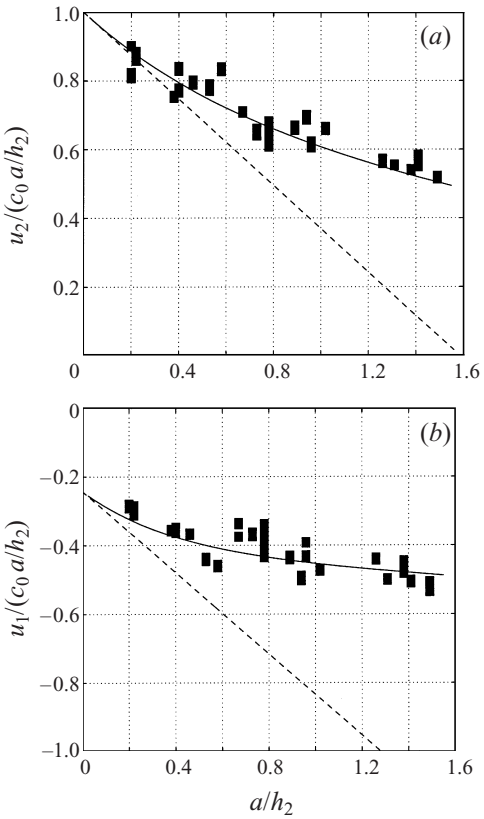


FIGURE 4. Horizontal velocities at the maximal displacement of the wave vs non-dimensional amplitude a/h_2. Maximal amplitude $a_{max}/h_2 \simeq 1.55$. Squares: measurements. Solid line: fully nonlinear theory. Dashed line: KdV theory, (3.10)–(3.11). (*a*) Velocity in the upper layer, $u_2(y = h_2/2)$. (*b*) Velocity in the lower layer, $u_1(y = -a^-)$. For KdV theory: $u_1(y = 0^-)$.

relevant to give a few results for larger depth ratio to provide a somewhat bigger picture. We give in this case theoretical results for $u_2(y = h_2/2)$ and $u_1(y = -a^-)$ for $h_1/h_2 = 10$ and $h_1/h_2 = 100$, without performing experiments, see figure 5. The fully nonlinear model and the KdV model compare well for small a/h_2. This is true even for $h_1/h_2 = 100$, where the KdV model is not expected to be valid.

We note that the velocity in the upper layer is relatively little influenced by an increased depth of the lower layer, when a/h_2 is held fixed.

It is of interest to compare our results for $u_2(y = h_2/2)$ in figures 4–5, obtained for

https://doi.org/10.1017/S0022112098003528 Published online by Cambridge University Press

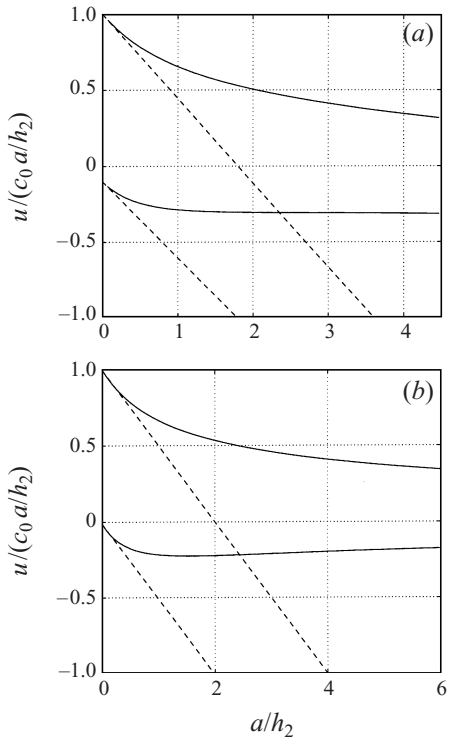


FIGURE 5. Horizontal velocities at the maximal displacement of the wave vs non-dimensional amplitude a/h_2. Upper line in each figure: $u_2(y = h_2/2)$, lower line $u_1(y = -a^-)$. For KdV theory: $u_1(y = 0^-)$. Solid line: fully nonlinear theory. Dashed line: KdV theory (3.10)–(3.11). (*a*) $h_1/h_2 = 10$ ($a_{max}/h_2 \simeq 4.45$). (*b*) $h_1/h_2 = 100$ ($a_{max}/h_2 \simeq 49.2$).

the depth ratios $h_1/h_2 = 4.13$, 10 and 100, with similar results obtained by Kao *et al.* (1985, figure 10). They used hot-film probes to measure the maximal fluid velocity in the upper layer and applied depth ratios $h_1/h_2 = 6$, 13, 19. They found that $u_2/c_0 = a/h_2$, i.e. that $(u_2/c_0)/(a/h_2) = 1$, for $a/h_2 < 1$ for all depth ratios tested. They noted a progressive deviation as a/h_2 increased beyond 1, however. On this point our results give evidence of a more precise description of the induced velocities in the fluids. The results here in figures 4 and 5 clearly document that $u_2/(c_0 a/h_2)$ deviates from and is significantly less than unity for moderate and large a/h_2.

Our results support, on the other hand, one of the main conclusions of Kao *et al.*, namely that KdV theory for interfacial solitary waves is appropriate in a fluid of finite total depth, for small a/h_2, for all depth ratios considered.

5. Propagation velocity

Besides applying the particle imaging system for velocity measurements, the individual pictures from the recordings are also useful for a visual determination of the position of the pycnocline. The pycnocline is visualized in these experiments due to the higher concentration of particles there than elsewhere. We use this method to determine the propagation velocity of a solitary wave, based on recordings at two sections which in the laboratory are separated by 5.9 m. Considering first the motion at the central part of recording section 1, we determine the (x_1, y_1) coordinates of the

https://doi.org/10.1017/S0022112098003528 Published online by Cambridge University Press

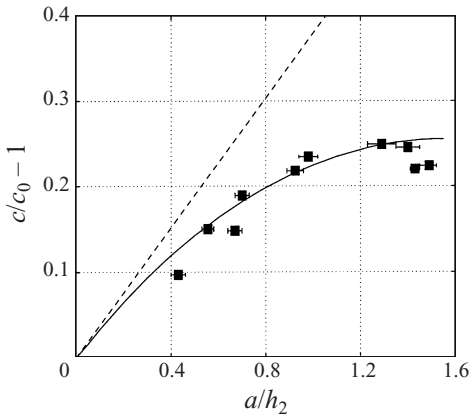


FIGURE 6. Excess propagation speed $c/c_0 - 1$ vs amplitude. Maximal amplitude $a_{max}/h_2 \simeq 1.55$. Squares: measurements. Horizontal bars indicate drop in amplitude between recording sections. Solid line: fully nonlinear theory. Dashed line: KdV theory (3.7).

pycnocline and time t_1 when the slope at the leading part of the wave is steepest. The procedure is repeated for recording section 2, where the horizontal coordinate x_2 and time t_2 are determined when the pycnocline is at y_1, the same level as in section 1. The velocity is then found by dividing the distance by the elapsed time. The accuracy of this method is determined approximately by the thickness of the pycnocline divided by its slope times the distance between the recording sections. The method is always quite good for moderate to large wave amplitude. The measurements of c are presented in figure 6 where the reference speed c_0 is determined theoretically from (3.8). The velocity measurements compare excellently with the fully nonlinear theory up to the maximal velocity. Again the KdV model, with c determined by (3.7), is useful for small a/h_2. We find that the wave amplitude undergoes a reduction of up to about 8% between the test sections, as indicated by the horizontal bars in the figure.

All measurements of the propagation velocity are performed for wave amplitude considerably larger than the pycnocline thickness. We have also performed a few runs with amplitude of the order of the pycnocline thickness (results not shown). With a small slope of the wave it becomes more difficult to determine the velocity precisely. We observe, however, a slower velocity than predicted by the two-layer model.

6. Wave profile

Having determined the propagation velocity we are now able to determine the wave profile. Based on a sequence of pictures we measure the vertical coordinate as function of time at a certain horizontal position in the recording section. Two different procedures are applied: (i) by measuring the vertical coordinate where there is a jump in the velocity, and (ii) by visual determination of the position of the pycnocline. The resulting profiles are shown in figure 7(*a–d*), for wave amplitude in the interval $a/h_2 = 0.22$ to 1.23. Comparison is also made with the fully nonlinear two-layer model, with excellent agreement for all cases.

In figure 7(*e*) the profile of a wave with almost maximal amplitude is displayed (cases A and C as described in §4.1). The leading part of the wave profile exhibits very good agreement with the theoretical computations. Rolls due to the Kelvin–

https://doi.org/10.1017/S0022112098003528 Published online by Cambridge University Press

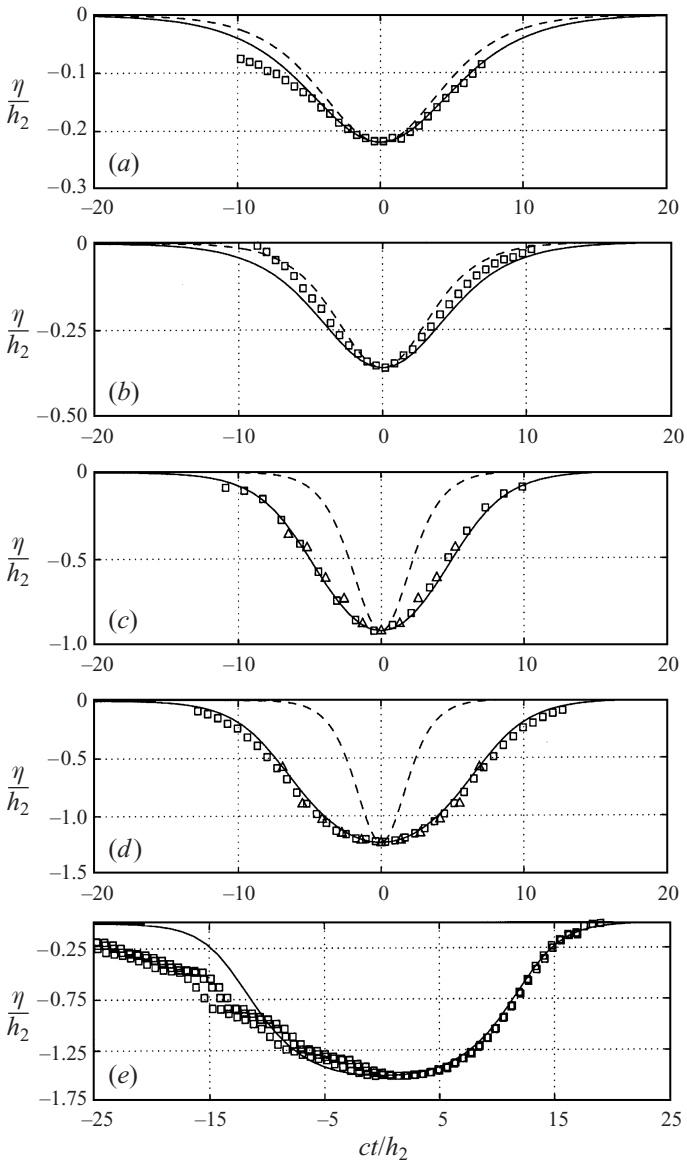


FIGURE 7. Wave profile $\eta(ct)$ at fixed position at camera 2 (10.5 m). Squares: measured pycnocline. Triangles: measured jump in velocity. Solid line: fully nonlinear theory. Dashed line: KdV theory (3.6). (*a*) $a/h_2 = 0.22$. (*b*) $a/h_2 = 0.36$. (*c*) $a/h_2 = 0.91$. (*d*) $a/h_2 = 1.23$. (*e*) $a/h_2 = 1.51$.

Helmholtz instability develop behind the maximal displacement of the wave, and the motion becomes rather violent in the vicinity of the pycnocline which is smeared out. The tail of the wave does not fit well with the theory. (We note that the initial volume generating the wave in figure 7 *e* is twice that of the wave in figure 7 *d*.)

We also investigate the horizontal velocity in the upper layer, i.e. $u_2(y = h_2/2)$, as function of time, see figure 8. There is again very good agreement between the experiments and the nonlinear theory.

The overall good agreement between the experimental and the theoretical wave shape means that the two approaches will agree also with regard to the relation

https://doi.org/10.1017/S0022112098003528 Published online by Cambridge University Press

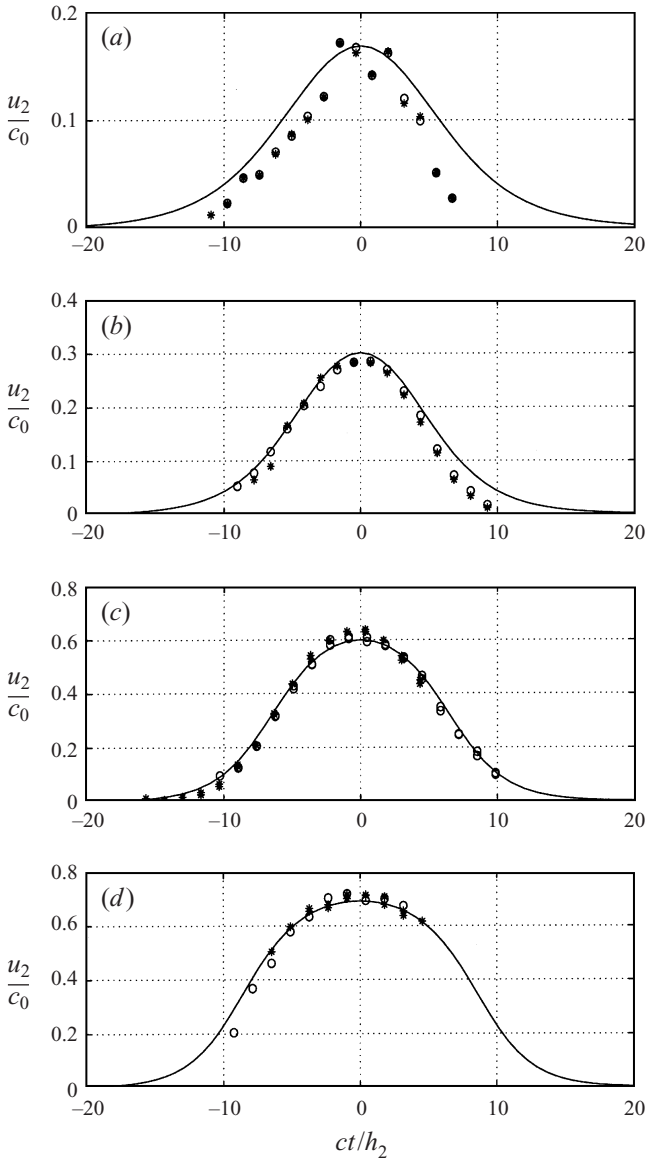


FIGURE 8. Horizonal velocity u_2 in upper layer at $y = h_2/2$ and fixed x as funtion of ct/h_2. Measurements at camera 1 (stars) and at camera 2 (circles). Solid line: fully nonlinear theory. (*a*) $a/h_2 = 0.22$. (*b*) $a/h_2 = 0.36$. (*c*) $a/h_2 = 0.91$. (*d*) $a/h_2 = 1.23$.

between the wavelength and amplitude. We have previously investigated this relationship in an example where we compare our nonlinear model with selected experiments by Koop & Butler (1981), see Grue *et al.* (1997, figure 3).

7. Conclusion

We have investigated properties of solitary waves propagating in a two-layer fluid comparing experiments and theory. In the experiments the velocity field induced by the waves, the propagation speed and the wave shape are quite accurately measured using particle tracking velocimetry and image analysis. We use fresh water above salt

https://doi.org/10.1017/S0022112098003528 Published online by Cambridge University Press

water with a ratio of 4.13 between the lower and upper layer. The wave amplitudes range from a small value up to almost maximal amplitude. The thickness of the pycnocline is in most experiments about 0.13 times the depth of the thinner layer, but some experiments are also performed with a relative pycnocline thickness up to about twice this value.

The theoretical models include a fully nonlinear interface model and a KdV model. With the fully nonlinear model available we here only consider KdV theory to leading order in the displacement of the interface. The fully nonlinear model compares excellently with the experiments for all quantities measured. This is true for the whole amplitude range, even for a pycnocline which is not very sharp (figures 2–8). In the experiments with the largest waves, rolls due to the Kelvin–Helmholtz instability develop behind the maximal displacement of the wave. The pycnocline is then locally smeared out. We still find good agreement between the experiment and the fully nonlinear theory, except for the profile at the tail of the wave, and for the unstable motion in the pycnocline. When instability occurs, it is evident that the destabilizing effect of an unstable velocity profile dominates the stabilizing effect of the stable density profile. We evaluate the local Richardson number and find that the occurrence of instability is roughly in agreement with the theorem of Miles and Howard.

Experimental confirmation of the KdV theory for long waves with small amplitudes has been obtained earlier, see e.g. Koop & Butler (1981), Segur & Hammack (1982) and Kao *et al.* (1985). The results in the last reference indicate that KdV theory is valid also for moderate and rather large amplitude. At this point our results give evidence of a more precise description of the induced velocities in the fluids. We find here that KdV theory is useful for wave amplitude up to about 0.4 times the depth of the thinner layer (figures 2, 7 and 8). The comparisons in figures 4–6 show, however, that the KdV theory systematically deviates from the experiments and the fully nonlinear theory for moderate and large amplitude.

The KdV theory is found to be useful for all depth ratios considered (when the wave amplitude is small). This was also the conclusion of Kao *et al.* (1985). Somewhat surprisingly, this result is true even for $h_1/h_2 = 100$ (figure 5*b*).

Segur & Hammack and Kao *et al.* performed experiments with initial conditions generating either a single or several solitary waves. In the latter reference a train with as many as seven solitary waves was generated. The number of solitary waves generated depends both on the initial volume and its depth to length ratio. In our experiments we have by careful adjustment of the length and depth of the initial volume always generated a single solitary wave. This is also true in the experiments with the largest waves.

The accuracy of the measurements is demonstrated in figures 2(*c*) and 4(*a*,*b*), in particular. The maximal deviation in the measured u/c_0, from a mean value of the experiments, and from the computations using the theoretical model, is about 5% in figure 2(*c*) and about 7–8% in figure 4(*a*, *b*), in approximate agreement with the error analysis described in §2.3. A more careful calibration of the experiments, a smaller shutter speed and a higher resolution of the cameras will enhance the accuracy.

The skillful technical assistance by Mr Arve Kvalheim and Mr Svein Vesterby is gratefully acknowledged. This work was conducted under the Strategic University Programme 'General Analysis of Realistic Ocean Waves' funded by the Research Council of Norway.

https://doi.org/10.1017/S0022112098003528 Published online by Cambridge University Press

Appendix A. Numerical procedure for the fully nonlinear two-layer model

Symmetric wave profiles with respect to $x = 0$ are considered. Symmetry about $x = 0$ may be expressed by $z(-x) = -z^*(x)$. Let I_+ denote the part of I where $x \geqslant 0$. Equations (3.3) and (3.4) now read

$$\pi(\gamma_1' + cx_\xi') = \mathrm{PV}\int_{I_+} \mathrm{Re}\left(\frac{z_\xi'}{z'-z}\right) cy_\xi \mathrm{d}\xi - \int_{I_+} \mathrm{Re}\left(\frac{z_\xi'}{z'+z^*}\right) cy_\xi \mathrm{d}\xi$$
$$- \int_{I_+} \mathrm{Re}\left(\frac{z_\xi'}{z^*-2\mathrm{i}h_1-z'} + \frac{z_\xi'}{z+2\mathrm{i}h_1+z'}\right) cy_\xi \mathrm{d}\xi$$
$$+ \int_{I_+} \mathrm{Im}\left(\frac{z_\xi'}{z'-z} + \frac{z_\xi'}{z'+z^*} + \frac{z_\xi'}{z^*-2\mathrm{i}h_1-z'} - \frac{z_\xi'}{z+2\mathrm{i}h_1+z'}\right)(\gamma_1 + cx_\xi)\mathrm{d}\xi, \tag{A 1}$$

$$-\pi(\gamma_2' + cx_\xi') = \mathrm{PV}\int_{I_+} \mathrm{Re}\left(\frac{z_\xi'}{z'-z}\right) cy_\xi \mathrm{d}\xi - \int_{I_+} \mathrm{Re}\left(\frac{z_\xi'}{z'+z^*}\right) cy_\xi \mathrm{d}\xi$$
$$- \int_{I_+} \mathrm{Re}\left(\frac{z_\xi'}{z^*+2\mathrm{i}h_2-z'} + \frac{z_\xi'}{z-2\mathrm{i}h_2+z'}\right) cy_\xi \mathrm{d}\xi$$
$$+ \int_{I_+} \mathrm{Im}\left(\frac{z_\xi'}{z'-z} + \frac{z_\xi'}{z'+z^*} + \frac{z_\xi'}{z^*+2\mathrm{i}h_2-z'} - \frac{z_\xi'}{z-2\mathrm{i}h_2+z'}\right)(\gamma_2 + cx_\xi)\mathrm{d}\xi \tag{A 2}$$

for z' at I_+.

The interface I_+ is discretized by N points, $\xi = 1, 2, 3, \ldots, N$. Following Dold & Peregrine (1985), the principal value integrals are evaluated by expanding the integrand in a series in the vicinity of the pole at $z' = z$, and then integrating using the trapezoidal rule. The trapezoidal rule is also applied to the regular integrals. Taking into account the symmetry of y, γ_1 and γ_2, and the antisymmetry of y_ξ, the discrete counterparts of integral equations (A 1) and (A 2) may be written

$$\pi\left(\gamma_1(\xi') + cx_\xi(\xi')\right) = c\sum_{\xi=1}^{N}\left(\mathscr{A}(\xi',\xi) - \mathscr{A}_1(\xi',\xi)\right) y_\xi(\xi) - cy_{\xi\xi}(\xi')$$
$$+ \sum_{\xi=1}^{N}\left(\mathscr{B}(\xi',\xi) - \mathscr{B}_1(\xi',\xi)\right)\left(\gamma_1(\xi) + cx_\xi(\xi)\right), \tag{A 3}$$

$$-\pi\left(\gamma_2(\xi') + cx_\xi(\xi')\right) = c\sum_{\xi=1}^{N}\left(\mathscr{A}(\xi',\xi) - \mathscr{A}_2(\xi',\xi)\right) y_\xi(\xi) - cy_{\xi\xi}(\xi')$$
$$+ \sum_{\xi=1}^{N}\left(\mathscr{B}(\xi',\xi) - \mathscr{B}_2(\xi',\xi)\right)\left(\gamma_2(\xi) + cx_\xi(\xi)\right), \tag{A 4}$$

where

$$\mathscr{A}(\xi',\xi) + \mathrm{i}\mathscr{B}(\xi',\xi) = \begin{cases} z_{\xi\xi}/2z_\xi, & \xi = \xi' = 1 \\ \frac{1}{2}\left[z_\xi'/(z'-z) - \left(z_\xi'/(z'+z^*)\right)^*\right], & \xi = 1,\ \xi' > 1 \\ z_\xi'/(z'-z) - \left(z_\xi'/(z'+z^*)\right)^*, & \xi > 1,\ \xi' \neq \xi \\ z_{\xi\xi}/2z_\xi - \left(z_\xi'/(z'+z^*)\right)^*, & \xi > 1,\ \xi' = \xi \end{cases} \tag{A 5}$$

https://doi.org/10.1017/S0022112098003528 Published online by Cambridge University Press

and

$$\mathscr{A}_k(\xi',\xi) - \mathrm{i}\mathscr{B}_k(\xi',\xi) = \begin{cases} \frac{1}{2}(z'_\xi/(z^* - z' + 2(-1)^k \mathrm{i}h_k) - (z'_\xi/(-z - z' + 2(-1)^k \mathrm{i}h_k))^*), & \xi = 1 \\ z'_\xi/(z^* - z' + 2(-1)^k \mathrm{i}h_k) - (z'_\xi/(-z - z' + 2(-1)^k \mathrm{i}h_k))^*, & \xi > 1 \end{cases} \quad (A\,6)$$

for $k = 1, 2$. The discrete dynamic condition at the interface reads

$$\frac{1}{2|z_\xi(\xi)|^2}\left(\gamma_1^2(\xi) - \mu\gamma_2^2(\xi)\right) - \tfrac{1}{2}(1-\mu)c^2 + (1-\mu)gy(\xi) = 0, \qquad \xi = 1, \ldots, N, \quad (A\,7)$$

where $\mu = \rho_2/\rho_1$. In the present calculations an equidistant distribution in x is used which means that $x(\xi)$ is specified. In other cases, e.g. when calculating very steep or overhanging waves, it is convenient to distribute the points equally spaced along the arc length. Then $x(\xi)$ becomes part of the solution, on the other hand.

The derivatives with respect to ξ are obtained by a five-point Lagrangian differentiation formula. The first and second derivatives of a function $f(\xi)$ are then obtained by

$$f_\xi(\xi) = \tfrac{1}{12}\left(-f(\xi+2) + 8f(\xi+1) - 8f(\xi-1) + f(\xi-2)\right), \quad (A\,8)$$

$$f_{\xi\xi}(\xi) = \tfrac{1}{12}\left(-f(\xi+2) + 16f(\xi+1) - 30f(\xi) + 16f(\xi-1) - f(\xi-2)\right). \quad (A\,9)$$

At the truncation of the interface we replace equations (A 3) and (A 4) by $y(N) = 0$ and $y_{\xi\xi}(N) = 0$. We also require that the interface has horizontal tangent at $x(N)$, i.e. $y_\xi(N) = 0$. Calculations with various truncation are performed.

We now have $3N$ equations for the $3N + 1$ unknowns $\gamma_1(\xi)$, $\gamma_2(\xi)$, $y(\xi)$ and c (μ is assumed fixed, although it technically may be seen as part of the solution). In order to close the set of equations we either give the amplitude a or the volume of the solitary wave. The procedure is started by prescribing a small a and solving the equations iteratively with an appropriate weakly nonlinear start guess. We then continue by stepwise specifying the volume, solving the equations using Newton–Rapson's method, with a numerical approximation of the Jacobian matrix, and with initial guess extrapolated from the previous solution(s).

REFERENCES

Adrian, R. J. 1991 Particle-imaging techniques for experimental fluid mechanics. *Ann. Rev. Fluid Mech.* **23**, 261.

Amick, C. J. & Turner, R. E. L. 1986 A global theory of internal solitary waves in two-fluid systems. *Trans. Am. Math. Soc.* **298**, 431.

Apel, J. R., Holbrook, J. R., Liu, A. K. & Tsai, J. 1985 The Sulu Sea internal soliton experiment. *J. Phys. Oceanogr.* **15**, 1625.

Benjamin, T. B. 1967 Internal waves of permanent form in fluids of great depth. *J. Fluid Mech.* **29**, 559.

Dalziel, S. B. 1992 Decay of rotating turbulence: some particle tracking experiments. *Appl. Sci. Res.* **49**, 217.

Dold, J. W. & Peregrine, D. H. 1985 An efficient boundary-integral equation method for steep unsteady water waves. In *Numerical Methods for Fluid Dynamics*, vol. 2 (ed. K. W. Morton & M. J. Baines), pp. 671–670. Clarendon.

Evans, W. A. B. & Ford, M. J. 1996 An integral equation approach to internal (2-layer) solitary waves. *Phys. Fluids* **8**, 2032.

Farmer, D. M. & Smith, J. D. 1980 Tidal interaction of stratified flow with a sill in Knight Inlet. *Deep-Sea Res.* **27A**, 239.

Fjeldstad, J. E. 1964 Internal waves of tidal origin. Part I. Theory and analysis of observations. *Geof. Publ.* **XXV**, No 5, 1.

https://doi.org/10.1017/S0022112098003528 Published online by Cambridge University Press

Gjevik, B. & Høst, S. E. 1984 Langkammede indre bølger i Skagerak. *Naturen* **6**, 209.

Grue, J., Friis, A., Palm, E. & Rusås, P. O. 1997 A method for computing unsteady fully nonlinear interfacial waves. *J. Fluid Mech.* **351**, 223.

Hichcock, F. L. 1941 The distribution of a product from several sources to numerous localities. *J. Math. and Phys.* **20**, 224.

Holyer, J. Y. 1979 Large amplitude progressive interfacial waves. *J. Fluid Mech.* **93**, 433.

Howard, L. N. 1961 Note on a paper by John W. Miles. *J. Fluid Mech.* **10**, 509.

Kao, T. W., Pan, F.-S. & Renouard, D. 1985 Internal solitons on the pycnocline: generation, propagation, and shoaling and breaking over a slope. *J. Fluid Mech.* **159**, 19.

Keulegan, G. H. 1953 Characteristics of internal solitary waves. *J. Res. Natl Bureau of Standards* **51**, 133.

Koop, C. G. & Butler, G. 1981 An investigation on internal solitary waves in a two-fluid system. *J. Fluid Mech.* **112**, 225.

Kubota, T., Ko, D. R. S. & Dobbs, L.D. 1978 Weakly-nonlinear, long internal gravity waves in stratified fluids of finite depth. *J. Hydronautics* **12**, 157.

Long, R. R. 1956 Solitary waves in one and two fluid systems. *Tellus* **8**, 460.

Meiron, D. I. & Saffman, P. G. 1983 Overhanging interfacial gravity waves of large amplitude. *J. Fluid Mech.* **120**, 213.

Melville, W. K. & Helfrich, K. R. 1987 Transcritical two-layer flow over topography. *J. Fluid Mech.* **178**, 31.

Miles, J. W. 1961 On stability of heterogeneous shear flows. *J. Fluid Mech.* **10**, 496.

Ono, H. 1975 Algebraic solitary waves in stratified fluids. *J. Phys. Soc. Japan* **39**, 1082.

Segur, H. & Hammack, J. L. 1982 Soliton models of long internal waves. *J. Fluid Mech.* **118**, 285.

Sveen, J. K., Jensen, A. & Grue, J. 1998 Measurements of velocity fields in internal gravity waves. Documentation of experimental method. *Preprint series, Department of Mathmatics, University of Oslo*.

Turner, R. E. L. & Vanden-Broeck, J.-M. 1986 The limiting configuration of interfacial gravity waves. *Phys. Fluids* **29**, 372.

Turner, R. E. L. & Vanden-Broeck, J.-M. 1988 Broadening of interfacial solitary waves. *Phys. Fluids* **31**, 2486.

https://doi.org/10.1017/S0022112098003528 Published online by Cambridge University Press